Parameterization of Solar Fluxes over Mountain Surfaces for Application to Climate Models

Wei-Liang Lee[1], K. N. Liou[2], and Alex Hall[2]

[1]Research Center for Environmental Changes, Academia Sinica, Taipei, Taiwan

[2]Joint Institute for Regional Earth System Science and Engineering and Department of Atmospheric and Oceanic Sciences, University of California, Los Angeles, CA, USA

Abstract

On the basis of 3-D Monte Carlo photon tracing simulations, we have developed a parameterization of solar fluxes over mountain surfaces by means of the multiple linear regression analysis associated with topographic information, including elevation, solar incident angle, sky view factor, and terrain configuration factor. For clear skies without aerosols and clouds, the regression equation for the direct flux can explain more than 98% of the variation in which the solar incident angle is the dominant factor, except when the sun is very low or at zenith. About 60% of the variation in the diffuse flux is predicted by the regression equation in which the mean elevation, sky view factor, and solar incident angle are key factors. The terrain-reflected fluxes, proportional to the surface albedo, are well correlated with the terrain configuration factor with more than 80% of the variation that can be explained. The coupled fluxes involve intricate interactions, and the regression analysis is less satisfactory in cases of low albedo values. However, over high-albedo surfaces, the terrain configuration factor becomes most dominant, leading to a significant improvement in regression performance. In these analyses, a surface albedo invariant with wavelength has been used. Using a region over the Sierra Nevada as a testbed, the preceding regression parameterizations have been specifically developed so that the fluxes evaluated from the 3-D Monte Carlo model over intense topography can be used as a perturbation term to correct those computed from the plane-parallel counterpart, commonly used in regional climate models and GCMs.

1. Introduction

The spatial and temporal distribution of the surface solar radiation is critical to many processes including snowmelt, soil moistening, photosynthesis, and evapotranspiration [*Geiger*, 1965; *Bonan*, 2002; *Gu et al*., 2002; *Müller and Scherer*, 2005]. It results from interactions between the direct and diffuse solar beams and the surface. Because of the complexity of spatial orientation and optical properties of the surface, quantifying these interactions and hence surface fluxes has been very difficult.

A number of models with a varying degree of sophistication have been developed to evaluate surface solar fluxes over mountainous areas [*Hay and McKay*, 1985; *Duguay*, 1993]. In these models, the direct solar flux was calculated by employing the correction based on the cosine of solar incident angle, and considering the shadow effect caused by nearby mountains [e.g., *Olyphant*, 1986]. The diffuse solar flux has been modeled as being proportional to the sky view factor, which is the portion of sky dome visible to the target [*Dozier and Frew*, 1990]. Factors contributing to the terrain-reflected flux have generally not been considered explicitly, but are approximated by assuming a first-order reflection between surrounding terrain and the target surface [e.g., *Dubayah et al*., 1990]. *Miesch et al*. [1999] further investigated this issue using a Monte Carlo approach over a 2-D rugged terrain to calculate surface solar fluxes, and concluded that a 10% error can occur if the terrain effect is not accounted for.

Parameterizations using topographic information have been developed to calculate solar radiation over mountainous surfaces [e.g. *Dubayah et al*., 1990; *Essery and Marks*, 2007]. However, as pointed out by *Dubayah and Rich* [1995], the sky view factor is calculated assuming that diffuse radiation is isotropic. Employing empirical directional distribution of diffuse intensity, *Wang et al*. [2005] found that substantial errors could be produced if the anisotropic nature of diffuse radiation is not considered. The angular distribution of the diffuse radiance, which is strongly dependent on the atmospheric conditions, cannot be accurately resolved by conventional radiative transfer schemes in climate models. In these parameterizations, reflected radiation is generally proportional to the surrounding mountain areas visible by the target. However, some of these areas may have already been shaded and receive very little or no reflected radiation. Moreover, these simplified approaches do not account for the effect of multiple reflections, which is particularly important over snow surfaces and steep valleys [*Dozier*, 1980]. In view of above, a more sophisticated 3-D radiative transfer approach should be utilized to develop a more accurate parameterization.

Chen et al. [2006] developed a 3-D Monte Carlo radiative transfer model to calculate solar fluxes exactly over mountains in a clear sky atmosphere and found that the reflected radiation can account for 3% of the total surface fluxes during the winter time with a high surface albedo. They also showed differences in the surface solar flux ranging from 5 to 20 W/m^2 between mountainous and unobstructed horizontal surfaces with the same mean elevation. *Liou et al*. [2007] utilized this

3-D model to evaluate the surface fluxes over the Tibetan Plateau and illustrated that anomalies of the surface solar flux with reference to a horizontal surface can be as large as 600 W/m^2 in shaded areas. The domain-average solar surface flux over a regional model scale (e.g., 50×50 km^2) with intense topography can deviate from the smoothed surface by 10−50 W/m^2. Although the 3-D Monte Carlo photon tracing program might be the most accurate method for radiative transfer calculation involving mountains, however, this approach is computationally expensive, and its direct implementation in a climate model would not be practical.

In this study, we developed a parameterization of surface solar fluxes based on the results from a 3-D Monte Carlo simulation using the intense topography of the Sierra Nevada as our test bed. Employing sub-grid-scale topographic parameters as independent variables, multiple linear regression analysis can be carried out to evaluate surface solar fluxes. Given the information about topography, a more accurate and physically-based surface solar flux can be predicted from the resulting simple linear regression equations. In current regional climate models and GCMs, conventional 1-D radiative transfer schemes assuming an unobstructed horizontal surface are typically used to compute solar fluxes. For this reason, we develop a parameterization that predicts flux deviations over mountains from the horizontal surface counterpart. Having the direct and diffuse fluxes calculated by a plane-parallel radiative transfer scheme, along with solar incident angle and terrain information (e.g., the sky view factor, terrain configuration factor, etc.) as inputs

variables, the present parameterization can be utilized to evaluate the solar fluxes received by mountain surfaces more reliably and accurately for use in climate models.

The presence of clouds could significantly alter the distribution of surface solar fluxes. However, the spatial and temporal variations in clouds are very large, and the optical properties of clouds are modulated by numerous variables, including cloud optical depth and height, as well as the size and shape spectra of cloud particles. In order to focus on the effect of complex topography on surface solar fluxes, we have designed parameterization of these fluxes primarily for clear sky conditions. Although the annual mean of global average cloud amount over land is 54% [*Warren et al*., 2007], this parameterization should be valid for the direct flux and could provide first-order estimate for diffuse and reflected-related fluxes.

This paper is organized as follows: A brief introduction to the 3-D Monte Carlo photon tracing program with the new surface configuration is given in Section 2. The various categories of downward solar fluxes to be predicted, and several relevant topographic parameters to be used as independent variables, such as the solar incident angle, the sky view factor, and the terrain configuration factor, are described in Section 3. In Section 4 we present the results of the multiple linear regression for various solar flux components. In addition, we show the impact of topographic variables on flux variations and their relative importance. Application of the present parameterization to climate models and its compatibility to various domain sizes and atmospheric

conditions are discussed in Section 5. Conclusions are given in Section 6.

2. 3-D Radiative Transfer Model for Surface Solar Flux Calculations

The Monte Carlo approach used in this study generally follows the model developed by *Chen et al*. [2006], except for the land surface configuration. Therefore, only a brief description is given here. In the current approach, the atmospheric domain is divided into finite cuboid cells such that the optical properties are homogeneous within each cell. Photons entering the top of the atmosphere (TOA) are defined by unit irradiance, and their direction is given by the position of the sun. The optical path length l, which a photon travels from the TOA to its first encounter with an air molecule, or between two encounters with an air molecule, is determined by Beer's law: $l = -\ln \xi$, where ξ is a random number uniformly distributed within the interval [0,1]. When a photon reaches the point of encounter, the probability it is absorbed or scattered is dependent on the single-scattering albedo, the ratio of the scattering cross-section to the extinction cross-section.

In the absorption case, the photon is terminated. However, if scattering occurs, the photon is deflected in a direction determined by the mean scattering phase function of the cell, which is a function of the incoming and outgoing directions characterized by μ (cosine of the zenith angle, θ) and φ, the azimuth angle. Once the photon hits the ground, the energy of the reflected photon is equal to the product of the energy of incoming photon and the surface albedo. To a good

approximation, the land surface can be taken as Lambertian for flux calculations, that is, the reflected flux is isotropic. The direction of the reflected photon is determined by $\mu' = \cos\theta' = \sqrt{\xi_1}$ and $\varphi' = 2\pi\xi_2$, where ξ_1 and ξ_2 are random numbers within the interval [0,1]; θ' and φ' are the zenith and azimuth angles relative to the inclined surface, respectively. Each photon is traced until it is absorbed by the atmosphere or leaves the TOA. The flux at each cell facet can be obtained by tallying the total weights of the photons crossing the cell's boundary.

In the development of a 3-D Monte Carlo photon tracing model, *Chen et al*. [2006] adopted a stair-like form to represent mountain surfaces. This approximation is computationally efficient and convenient for programming implementation. However, such surfaces can result in more reflection events than those on realistic inclined surfaces. For example, for a point on a horizontal facet very close to a vertical facet of the stair-like form, almost half of the sky dome is obstructed by the vertical facet. When a photon hits this point and is reflected, there is about 50% probability that this photon will then hit the vertical facet, leading to the occurrence of another reflection event. This effect can trap more energy at the corner between a horizontal and a vertical facet, producing a substantial surface flux. However, the presence of vertical cliffs is not very common for realistic land surfaces. Furthermore, because a slope is treated as a combination of a horizontal and a vertical facet in this approximation, the modeled surface area would be larger than the real surface area, resulting in underestimation of the surface radiative flux in the whole domain. Although the

preceding two effects might compensate each other in flux calculations over a large domain, it could produce significant errors locally.

In view of the above, we have developed a more realistic surface model using the following approach. In each pixel the surface is constructed by means of triangles based on the elevation data available from the digital elevation model (DEM). Using the method introduced by *Jenness* [2004], we connected the pixel's center point to the center points of eight surrounding pixels to generate eight 3-D triangles. Subsequently, the portions of those triangles residing within the pixel's boundaries are considered as the "real" topography of the pixel in the model. These triangles are also used to estimate the surface area of each pixel. As also shown by *Jenness* [2004], the area estimated from this method is close to that calculated by more sophisticated methods, such as the triangulated irregular network (TIN), for pixel numbers more than 250 in the domain.

In this study, we used the midlatitude climatalogical atmospheric profile with 70 layers from the mean sea level to 70 km. The vertical resolution varies from 5km near TOA to 100 m near the surface. While the vertical resolution can be altered arbitrarily, we found that surface fluxes are not sensitive to changes in vertical grid. Because our current effort has focused on developing a physically-based and workable parameterization for the sub-grid-scale terrain effect on surface solar fluxes, we have used clear sky conditions without aerosols for analysis. In this case, Rayleigh scattering is the only atmospheric scattering mechanism included in Monte Carlo simulations. In

Section 5.c, we have discussed the manner in which the current parameterization can be applied to variations in atmospheric gaseous profiles, aerosols, and clouds.

To test the accuracy of Monte Carlo photon tracing, 4×10^6 photons were first assigned to a 20×20 km^2 computational domain with a 1×1 km^2 resolution, so that approximately 10^4 photons are targeted toward each surface pixel. We then increased the number of photons by a factor of 10 (i.e., to 4×10^7), and found that the resulting relative difference in the mean surface flux is less than 0.3%. Thus, use of 10^4 photons per pixel should suffice to achieve accurate statistics, and this photon density is employed throughout this study.

The purpose of this study is to investigate the mountain effect; therefore, a uniform surface albedo value is used in Monte Carlo simulations, although we illustrate the sensitivity of fluxes involving terrain reflection to surface albedo by performing an additional set of Monte Carlo simulations with elevated—but still uniform—surface albedo. In this study, only one spectrally invariant surface albedo is used in all simulations. As shown in *Liou et al*. [2007], we have carried out a 3-D Monte Carlo experiment utilizing two MODIS albedo values for the visible (0.3-0.7 μm) and near-IR (0.7-5.0 μm) regions versus one spectrally invariant albedo in the shortwave region. Differences in surface broadband fluxes were shown to be less than 0.6 W/m^2, negligible in comparison to large anomalies between mountains and a flat surface, which are on the order of 100 W/m^2. For this reason and for the purpose of broadband flux calculation, we have used the

spectrally invariant albedo.

As the experiment test bed, we selected a rugged area of the Sierra Nevada in the Western United States, composed of a variety of elevations and slopes (Figure 1). The surface topography with a 1 km resolution was taken from the HYDRO1k geographic database available from the U. S. Geological Survey's (USGS) National Center for Earth Resources Observation and Science (EROS) data center. This area is divided into eighty 20×20 km^2 domains to represent the general terrain characteristics and topographical variations. Because the model design is cyclic at the domain boundary, photons exiting the western boundary will re-enter the domain at the eastern boundary. As a result, areas with low elevation near the eastern boundary could be shadowed by mountains at the western side. In order to reduce this edge effect, only the topographic information and surface radiative fluxes in the central 10×10 km^2 areas were used for parameterization. This domain size was chosen to be comparable to that of a regional climate simulation or operational weather forecast.

3. Variables for Multiple Linear Regression Analysis

As shown in previous studies [e.g. *Chen et al*., 2006], the direct, diffuse, and reflected solar fluxes are each controlled by different topographic variables. Thus, we have divided the surface solar fluxes into categories and perform regressions for each flux category separately. As illustrated

in Figure 2, the solar radiative fluxes can be categorized into five components according to the path of the photons that make them up: (1) Direct flux, denoted as F_{dir}, is composed of photons hitting the ground directly from the sun without encountering scattering or reflection; (2) Diffuse flux, denoted as F_{dif}, contains photons experiencing single or multiple scattering by air molecules, but never encountering surface reflection; (3) Direct-reflected flux, denoted as F_{rdir}, is comprised of unscattered photons reflected by nearby terrain; (4) Diffuse-reflected flux, denoted as F_{rdif}, is similar to direct-reflected flux, except that the photon is first scattered by air molecules and then reflected by nearby terrain; (5) Coupled flux, denoted as F_{coup}, represents photons that, after being reflected by the surface, encounter scattering, or one or more additional surface reflections. It is clear that the direct and diffuse fluxes are independent of surface albedo. Since F_{rdir} and F_{rdif} contain photons that have been reflected once, they are simply proportional to albedo. Only the coupled flux has nonlinear relationship with surface albedo. It is also noted that there will be no F_{rdir} and F_{rdif} on an unobstructed horizontal surface. In this study, the solar radiative flux received by mountain surfaces is defined as the total solar energy reaching the ground divided by the horizontal surface area instead of the mountain area. This definition is selected so that differences in the solar energy budget between mountainous and unobstructed horizontal surfaces can be compared in a consistent manner. It should also be noted that F_{dif} defined in this study differs from the diffuse flux defined in conventional radiative transfer schemes, which is the summation of F_{dif} and F_{coup} since

all reflected radiation, including upward and downward components, is considered as diffuse fluxes.

In current climate models, conventional plane-parallel radiative transfer schemes have already developed to calculate solar fluxes on a horizontal surface with a known elevation. Therefore, the purpose of the present parameterization effort is to produce relative deviations of the fluxes from those of an unobstructed horizontal surface, given sub-grid-scale topographic information. More specifically, the results of the multiple linear regression analysis done in this study are relative deviations of the five components of downward solar surface fluxes described above from those of an unobstructed horizontal surface with the same mean elevation using the broadband plane-parallel radiative transfer model developed by *Fu and Liou* [1992] and further improved by *Gu et al.*, [2003; 2006] for application to climate models and GCMs. For the direct, diffuse, and coupled fluxes, their corresponding relative deviations are defined as

$$F_i' = \frac{F_i - \hat{F}_i}{\hat{F}_i}, \quad i = \text{dir, dif, coup,} \tag{1}$$

where F_i are the surface fluxes over mountains calculated by the 3-D Monte Carlo model, and $\hat{F}_i$ are the fluxes with reference to the unobstructed horizontal surface. However, in the case of the direct- and diffuse-reflected fluxes, $\hat{F}_{\text{rdir}}$ and $\hat{F}_{\text{rdif}}$ are zeros so that Eq. (1) cannot be defined. For this reason, we set

$$F'_{\text{rdir}} = \frac{F_{\text{rdir}}}{\hat{F}_{\text{dir}}}, \text{and } F'_{\text{rdif}} = \frac{F_{\text{rdif}}}{\hat{F}_{\text{dif}}}. \tag{2}$$

To prepare the independent variables for regression, we introduce the concept of the sky view

factor and the terrain configuration factor, which are widely used in estimating the diffuse and reflected fluxes over mountainous areas, respectively. The sky view factor V_d was originally defined as the ratio of the diffuse flux received by a point to that received by an unobstructed horizontal surface [*Dubayah et al*., 1990]. However, because the geometry of diffuse radiation is dependent on the position of the sun and atmospheric conditions, calculating the sky view factor is computationally expensive and storage intensive. If one assumes that the diffuse flux is isotropic, the sky view factor becomes the portion of the sky dome visible to the target point as shown in Figure 2. This term can be obtained by calculating the area of unobstructed hemisphere given by [*Dozier and Frew*, 1990]

$$\begin{aligned} V_d &= \frac{1}{\pi}\int_0^{2\pi}\int_0^{H_\varphi} \sin\theta[\cos\theta\cos\theta_s + \sin\theta\sin\theta_s\cos(\varphi-\varphi_s)]d\theta d\varphi \\ &\approx \frac{1}{2\pi}\int_0^{2\pi}[\cos\theta_s\sin^2 H_\varphi + \sin\theta_s\cos(\varphi-\varphi_s)\times(H_\varphi - \sin H_\varphi\cos H_\varphi)]d\varphi, \end{aligned} \tag{3}$$

where θ_s is the slope, φ_s is the aspect of the slope, and H_φ is the horizon angle measured from the zenith down to the local horizon at the orientation direction φ, which can result either from "self-shadowing" by the slope itself or from nearby mountains.

The terrain configuration factor C_t, which is defined as the area of surrounding mountains visible to the target point, also shown in Figure 2, can be written as [*Dozier and Frew*, 1990]

$$\begin{aligned} C_t &= \frac{1}{\pi}\int_0^{2\pi}\int_{H_\varphi}^{\psi_\varphi} \sin\theta[\cos\theta\cos\theta_s + \sin\theta\sin\theta_s\cos(\varphi-\varphi_s)]d\theta d\varphi \\ &\approx \frac{1+\cos\theta_s}{2} - V_d, \end{aligned} \tag{4}$$

where ψ_φ is the angle of the ray parallel to the slope defined by

$$\tan\psi_\varphi = \frac{-1}{\tan\theta_s \cos(\varphi - \varphi_s)}. \tag{5}$$

On an unobstructed infinite slope, the direct solar flux is proportional to the cosine of the solar incident angle θ_i, which is defined as the angle between the direction of incident ray and the normal vector of the slope and can be expressed by

$$\cos\theta_i = \cos\theta_s \cos\theta_0 + \sin\theta_s \sin\theta_0 \cos(\varphi_s - \varphi_0), \tag{6}$$

where θ_0 and φ_0 are the solar zenith and azimuth angles, respectively. Defining $\mu_0 = \cos\theta_0$, and $\mu_i = \cos\theta_i$, the mean μ_i of the whole domain can be calculated by taking the spatial average of Eq. (6):

$$\begin{aligned} \langle\mu_i\rangle &= \mu_0\langle\cos\theta_s\rangle + \sin\theta_0\langle\sin\theta_s\cos(\varphi_s - \varphi_0)\rangle \\ &= \mu_0\langle\cos\theta_s\rangle + \sin\theta_0(\cos\varphi_0\langle\sin\theta_s\cos\varphi_s\rangle + \sin\varphi_0\langle\sin\theta_s\sin\varphi_s\rangle), \end{aligned} \tag{7}$$

where angle brackets denote spatial mean. Therefore, given the position of the sun, the average of μ_i for the whole domain can be determined if the means of $\cos\theta_s$, $\sin\theta_s\cos\varphi_s$, and $\sin\theta_s\sin\varphi_s$ are given.

In addition to the mean values for the sky view factor $\langle V_d\rangle$, the terrain configuration factor $\langle C_t\rangle$, and the cosine of the solar incident angle $\langle\mu_i\rangle$, conventional topographic parameters for each 10×10 km^2 domain, such as the mean elevation $\langle h\rangle$ and slope $\langle\theta_s\rangle$, are used. We also employed their standard deviation ($\sigma(h)$, $\sigma(\theta_s)$, $\sigma(V_d)$, $\sigma(C_t)$, and $\sigma(\mu_i)$) and skewness ($\gamma(h)$, $\gamma(\theta_s)$, $\gamma(V_d)$, $\gamma(C_t)$, and $\gamma(\mu_i)$) in the multiple linear regression analysis. In this manner, 15 independent variables are available for the regression analysis. The magnitudes of the independent variables vary substantially and the units associated with them may be different. Therefore, it is desirable to non-dimensionalize

the variables prior to performing the regression analysis. All independent variables are processed by first removing their means and then normalizing them by their respective standard deviations.

It should be noted that these variables are not necessarily orthogonal to each other. Since it is desirable to produce a parameterization with as few independent variables as possible, independent variables highly correlated to one another must be reduced to a single variable. To accomplish this, we first calculate correlation coefficients between each successive pair of variables. When the correlation coefficient between two variables is larger than 0.9, one of them will be removed. It turns out that some variables are indeed highly correlated. As implied by Eq. (4), the correlation coefficient between $\langle V_d \rangle$ and $\langle C_t \rangle$ is very close to -1. Also, $\langle \theta_s \rangle$ is highly correlated with $\langle C_t \rangle$ and therefore it is anti-correlated with $\langle V_d \rangle$. Furthermore, $\langle \theta_s \rangle$, $\langle V_d \rangle$, $\langle C_t \rangle$, and $\langle \mu_i \rangle$ are highly correlated with their standard deviations $\sigma(\theta_s)$, $\sigma(V_d)$, $\sigma(C_t)$, and $\sigma(\mu_i)$, respectively. As a result, the independent variables for the regression of F'_{dir} and F'_{dif} are $\langle h \rangle$, $\sigma(h)$, $\gamma(h)$, $\gamma(\theta_s)$, $\langle V_d \rangle$, $\gamma(V_d)$, $\langle \mu_i \rangle$, and $\gamma(\mu_i)$, while $\langle V_d \rangle$ and $\gamma(V_d)$ are replaced by $\langle C_t \rangle$ and $\gamma(C_t)$ for F'_{rdir}, F'_{rdif}, and F'_{coup} because C_t is originally designed for reflected-related fluxes. Also, note that when μ_0 is equal to 1, $\langle \mu_i \rangle$ is highly correlated to $\langle \theta_s \rangle$ since when the solar zenith angle is zero, θ_i is equal to θ_s according to Eq. (6). Therefore, when the sun is at the zenith, $\langle \mu_i \rangle$ and $\gamma(\mu_i)$ will be removed from the regression analysis.

4. Results of Parameterization

We choose seven different solar zenith angles (SZA) in this study, including μ_0 = 0.1, 0.25, 0.4, 0.55, 0.7, 0.85, and 1. For each SZA (except μ_0 = 1), four different solar azimuth angles (0º, 90º, 180º, and 270º) are applied for each of the 80 domains described at the end of Section 2. Therefore, there are 320 samples for each SZA (but only 80 samples for μ_0 = 1) to perform multiple linear regression. To obtain the simplest possible regression equation for each flux component, if the regression coefficients do not differ significantly from zero by using the *t*-test at the 90% confidence level, the corresponding independent variables are removed from regression equations. Since all independent variables are normalized, their associated regression coefficients represent the flux anomaly magnitude when the variable is increased by one standard deviation.

***a. Direct flux*:** The regression equation for deviation of the direct flux can be expressed by

$$F'_{\mathrm{dir}} = a_1 + b_{11}\langle\mu_i\rangle + b_{12}\langle V_d\rangle, \tag{8}$$

where a_1 is the intercept term, b_{11} and b_{12} are regression coefficients. Values of a and b for each μ_0 are listed in Table 1. The intercept term represents the mean deviations between mountainous and unobstructed horizontal surfaces. When the sun's position is very low, the shading effect leads to a 3% reduction in the direct flux, corresponding to a negative deviation of 1.5 W/m^2, though the mean deviation generally becomes insignificant when the sun is close to the zenith. The cosine of the solar incident angle is the dominant factor in direct flux calculations. A one standard deviation increase in $\langle\mu_i\rangle$ can lead to 31% and 2.7% increases for μ_0 = 0.1 and 0.85, respectively,

corresponding to 17 and 36 W/m^2 increases in the direct solar flux. $\langle V_d \rangle$ has negative impact on F'_{dir} with the sun very close to the horizon. However, the incoming flux becomes smaller in association with larger sky view factors as the position of the sun is higher.

To provide information about the explanatory power of the regression model, the left panels of Figure 3 compare the absolute values of the deviations in direct fluxes between the 3-D model and regression results for three values of μ_0. The coefficients of multiple determination R^2, listed in Table 2, are larger than 0.98 except for $\mu_0 = 0.1$ and 1, revealing that Eq. (8) can predict the direct flux quite accurately. The corresponding root mean square errors (RMSE) are generally less than 3 W/m^2, while it could reach 10 W/m^2 for $\mu_0 = 0.1$. Very small R^2 value when $\mu_0 = 1$ indicates that the direct flux is almost independent of $\langle \mu_i \rangle$ and $\langle V_d \rangle$. When the sun is at the zenith, there will be no shading effect at all; in this case, the variation of $\langle \mu_i \rangle$ is very small so that the direct flux cannot be explained by these two parameters. Even if all 8 independent variables mentioned in the end of Section 3 are used in the regression, R^2 is still smaller than 0.07, implying that the variation is rather random. Nevertheless, as shown in Figure 3, variation in the direct flux for $\mu_0 = 1$ is about 2 W/m^2, much smaller than variations in other cases, which are on the order of 100 W/m^2.

***b. Diffuse flux*:** The regression equation for deviation of the diffuse flux can be expressed by

$$F'_{\mathrm{dif}} = a_2 + b_{21}\langle h \rangle + b_{22}\langle \mu_i \rangle + b_{23}\langle V_d \rangle + b_{24}\gamma(h). \quad (9)$$

Values of the intercept and regression coefficients are also listed in Table 1. The most significant

factor determining deviation of the diffuse flux is the mean elevation, with which it is positively correlated. To understand the relationship between F'_{dif} and $\langle h \rangle$, we calculate the vertical distribution of the downward diffuse flux F_{dif} without topographic effect. As shown in Figure 4, the curves of downward diffuse fluxes are concave, and the curvature generally increases with increasing elevation. Therefore, for two domains with the same $\sigma(h)$ and $\gamma(h)$ but different $\langle h \rangle$, domain averaged deviations of the diffuse flux will be larger for the domain with larger $\langle h \rangle$. Furthermore, since the curves are concave, the domain with a positive $\gamma(h)$ will receive less diffuse fluxes than a domain with the same mean elevation but negative $\gamma(h)$. This will lead to anti-correlation between F'_{dif} and $\gamma(h)$, as shown in Table 1. However, there is an inflection point on the curve for $\mu_0 = 0.1$, leading to smaller regression coefficients for both $\langle h \rangle$ and $\gamma(h)$.

F'_{dif} also increases with increasing $\langle \mu_i \rangle$, illustrating the anisotropic nature of diffuse flux. Since the maxima of the phase function for Rayleigh scattering resides at the forward and backward directions for an unpolarized light beam, the majority of scattered photons move in the same direction as the direct solar beam, resulting in a positive correlation between F'_{dif} and $\langle \mu_i \rangle$. Even though the diffuse flux is anisotropic, the results determined from multiple linear regression display that F'_{dif} is largely proportional to the mean sky view factor based on the isotropic assumption, which has been used by many previous studies [e.g. *Dozier and Frew*, 1990]. The regression coefficients of $\langle V_d \rangle$ decrease as μ_0 increases, indicating that the shading effect becomes less

important when the sun is close to the zenith. On the other hand, the regression coefficients for $\langle \mu_i \rangle$ generally increase with increasing μ_0. These two effects compensate each other and lead to an almost constant R^2 on the order of 0.6 when $\langle \mu_i \rangle$ is less than 1.0, as listed in Table 2. Comparisons between the regression and simulation results are also shown in the right panels of Figure 3. The range of deviations in the diffuse flux is approximately 5 W/m^2, which is ~ 15% of the total. While the explanation power for F'_{dif} is smaller than that of F'_{dir}, RMSE of Eq. (9) for all μ_0 are all less than 0.5 W/m^2, smaller than those for Eq. (8).

***c. Direct- and diffuse-reflected fluxes*:** The regression equations for deviations of the direct-reflected and diffuse-reflected fluxes can be expressed, respectively, by

$$F'_{\mathrm{rdir}} = a_3 + b_{31}\langle C_t \rangle + b_{32}\langle h \rangle + b_{33}\gamma(h), \tag{10}$$

$$F'_{\mathrm{rdif}} = a_4 + b_{41}\langle C_t \rangle + b_{42}\langle h \rangle + b_{43}\gamma(h), \tag{11}$$

where the intercept terms and regression coefficients are listed in Table 3. Eqs. (10) and (11) can explain variation in the reflected fluxes quite well. Also noted in Table 2, the R^2 values for F'_{rdir} and F'_{rdif} are generally about 0.85 and 0.9, respectively, except when the sun is close to the horizon. Comparisons between the regression and simulation results are displayed in Figure 5. RMSE for F'_{rdir} and F'_{rdif} are 0.08-0.5 and 0.01 W/m^2, respectively. The intercept terms, which represent the mean responses, are always positive because these two fluxes are zero on an unobstructed horizontal surface. The dominant independent variable in the regression model for F'_{rdir} and F'_{rdif} is

the mean terrain configuration factor $\langle C_t \rangle$. The factor $\langle h \rangle$ also has a positive impact on F'_{rdir} and F'_{rdif} because the reflected photons encounter less absorption or scattering at a higher altitude before hitting the ground again. The negative regression coefficients for $\gamma(h)$ are a result of the fact that the extinction coefficient, which is proportional to the air density, increases as the elevation decreases. It is noted that the regression coefficients for F'_{rdir} and F'_{rdif} are very close, showing that the factors controlling variations in these two components are probably the same.

The variation in F'_{rdir} is ~ 1–8 W/m^2, depending on μ_0, whereas the variation in F'_{rdif} is ~ 0.3 W/m^2, as shown in Figure 5. It should be noted that F'_{rdir} and F'_{rdif} are functions of the surface albedo. Because F'_{rdir} and F'_{rdif} fluxes are composed of photons that undergo one reflection only, they are directly proportional to the surface albedo. In Eqs. (10) and (11), the regression coefficients were derived from 3-D Monte Carlo simulations for a surface albedo of 0.1. To obtain F'_{rdir} and F'_{rdif} with different albedo values, we can linearly scale these coefficients according to the new albedo value. For example, over the snow-covered surface with an albedo of 0.7, variations in F'_{rdir} and F'_{rdif} would be 7–56 and 2.1 W/m^2 (a factor of 7), respectively.

***d. Coupled flux*:** Deviation of the coupled flux can be expressed by the following regression equation:

$$F'_{\mathrm{coup}} = a_5 + b_{51}\langle \mu_i \rangle + b_{52}\langle C_t \rangle + b_{53}\langle h \rangle, \tag{12}$$

where the intercept term and the regression coefficients are listed in Table 4. From the values of R^2

listed in Table 2, we find that the explanation power of Eq. (12) is generally less than those for other flux components. The intercept terms are always negative. This is because the coupled flux is approximately the backscattering of the total energy reflected to the atmosphere. Because some reflected photons are intercepted by nearby mountains, the total amount of the coupled flux over rugged areas will be less than that over an unobstructed horizontal surface. Since the incoming direct and diffuse fluxes are positively correlated with $\langle \mu_i \rangle$, the total amount of the reflected solar energy should also be proportional to $\langle \mu_i \rangle$, leading to positive values of b_{51}. Additionally, F'_{rdir} and F'_{rdif} are independent of $\langle \mu_i \rangle$ so that the energy reflected back to the atmosphere, which can be estimated by subtracting F'_{rdir} and F'_{rdif} from the total reflected energy, is also proportional to $\langle \mu_i \rangle$. The negative regression coefficients for $\langle C_t \rangle$ indicate that the real physical mechanism determining F'_{coup} is the V_d, not C_t, since the backscattering effect dominates. Comparisons between the regression and simulation results are displayed in Figure 6, and it shows that variations in coupled fluxes are within 0.5 W/m^2 for this surface albedo value. Since the magnitude of variation is small, RMSE are generally less than 0.07 W/m^2.

The coupled flux is a nonlinear function of the surface albedo. For this reason, we have carried out an additional regression analysis using an albedo of 0.7. The intercept terms and regression coefficients are also listed in Table 4. As shown by R^2 in Table 2, the new regression equation can explain variation in the coupled flux much better than that with an albedo of 0.1. As

shown in Figure 6, the associated variations in the coupled flux can reach 8 W/m^2, much larger than that on a less-reflective surface, while RMSE also increase to 0.6 W/m^2. The most important factor becomes $\langle C_t \rangle$, and the regression coefficients for $\langle C_t \rangle$ and the intercept terms are all positive. Theses two facts reveal that as surface albedo increases, the effect due to multiple reflection becomes more dominant than that due to backscattering by the atmosphere. The impact of $\langle h \rangle$ on F'_{coup} is the same as on F'_{rdir} and F'_{rdif}, though this effect is not significant when albedo is 0.1. For practical application to climate models, several suitable albedo values can be selected for parameterization of the coupled fluxes, and regression parameters can be interpolated for intermediate albedo values.

5. Application of the Parameterization to Climate Models

a. *Improve the conventional radiative transfer scheme to account for 3-D mountain feature*. The conventional plane-parallel radiative transfer scheme in climate models generally can provide the direct and diffuse components of surface solar fluxes. Therefore, F'_{dir} and F'_{rdir}, can be computed by applying Eqs. (8) and (10) with the direct flux over an unobstructed horizontal surface given. However, it should be noted that the diffuse flux in those schemes is the summation of $\hat{F}_{\text{dif}}$ and $\hat{F}_{\text{coup}}$. Because the definition of the diffuse flux differs from the conventional one, one should conducted additional solar flux calculations using a conventional scheme with an albedo of zero to separate these two components. This will provide the diffuse flux without encountering reflections.

b. *Compatibility to different domain sizes*. The present parameterization has been developed for a 10×10 km^2 domain area representative of a grid cell of conventional mesoscale models. Our analysis has shown that a significant variation on the order of 100 W/m^2 could be produced at this scale. In order to investigate the mountain effect over a larger domain size, we have performed Monte Carlo simulations using 80 20×20 km^2, 36 30×30 km^2, and 16 50×50 km^2 domains in the Sierra Nevada area. The results show that the standard deviations of domain-averaged total surface fluxes are on the order of 13, 9, and 5 W/m^2 for 20×20, 30×30, and 50×50 km^2 domain sizes, respectively. Most of the variations were contributed by deviations of the direct flux, followed by the direct-reflected flux. Although variations in the direct flux could be compensated due to various orientations of mountain surfaces over larger domains, we show that deviations from 3-D structure must be accounted for at a resolution of 50×50 km^2.

To examine the compatibility of our parameterization at different scales, we have also calculated surface fluxes over larger domains using regression equations and compared them with the results simulated by the Monte Carlo approach. For example, a 20×20 km^2 domain can be separated into four 10×10 km^2 areas such that domain-average fluxes can be obtained by summing

all flux components corresponding to the four areas and applying parameterization. The resulting R^2 for F'_{dir}, F'_{rdir}, and F'_{rdif} for all three domain sizes are larger than 95%, except for F'_{dir} when the sun is at the zenith. The explanation power for F'_{coup} shows a rising trend as the domain size increases. The values of R^2 for F'_{coup} are within 0.42−0.71, 0.49−0.66, and 0.64−0.89 for domains with sizes of 20×20, 30×30, and 50×50 km^2, respectively. For F'_{dif}, however, R^2 at a domain size of 20×20 km^2 are only about 0.43, but it increases to 0.55 and 0.60 at domain sizes of 30×30 and 50×50 km^2, respectively.

In this study, the 1×1 km^2 resolution DEM from HYDRO1k was employed in 3-D Monte Carlo calculations. *Dubayah et al*. [1989] stated that surface solar fluxes could be sensitive to terrain spatial resolution and substantial errors could be produced with the size of grid cells larger than 200 m. Regarding the horizontal spatial scale, we would like to point out that "exact" 3-D radiative transfer calculations using the Monte Carlo photon tracing approach are extremely costly in terms of computational effort (computer time and analysis). Calculations employing fine geographical resolutions on the order of 100 m would be formidable for the entire region of 10×10 km^2. In order to understand differences in surface fluxes in a 10×10 km^2 domain caused by the input data for terrain configuration, we have carried out several experiments using the SRTM data [*Farr et al*., 2007] at a 3 arc second (~90 m) resolution over the same area corresponding to HYDRO1k. We selected 10 10×10 km^2 areas randomly and carried out 3-D Monte Carlo

calculations. We found that for these selected cases over the Sierra Nevada, differences between the resolution of 1 km and 90 m in F'_{dir} (~100 W/m^2), F'_{dif} (~10 W/m^2), and F'_{coup} (~1 W/m^2) for a 10×10 km^2 domain are generally less than 3%. Differences in F'_{rdir} (~8 W/m^2) and F'_{rdif} (<1 W/m^2) are much larger. Indeed, the spatial resolution issue requires further investigation.

c. *Application to different atmospheric conditions*. Although a mean atmospheric profile was used for all simulations, the present parameterization can be applied to different atmospheric compositions for the following reasons: First, variation in the trace gas concentrations only alters the absorption coefficient in association with the number of absorbed photons. Secondly, the number and direction of the scattered photons remain unchanged. And finally, because the effect due to change in the atmospheric absorption coefficient has already been determined in the conventional radiative transfer schemes, the present parameterization, which is in reference to deviations from the plane-parallel radiative transfer results, can be directly applied to different atmospheric conditions without modification [see Eqs. (1) and (2)].

The presence of aerosols and clouds could substantially alter the geometry of scattered photons. Therefore, the regression equations for F'_{dif}, F'_{rdif}, and F'_{coup} will need modifications. However, equations for F'_{dir} and F'_{rdir} will remain unchanged since only direct attenuation is involved. To apply the present regression-based parameterization to a background aerosol coupled with Rayleigh scattering, further numerical experiments would be require to account for variation in

the aerosol loading, e.g., using aerosol optical depth as an independent variable in the parameterization.

The effect of clouds on scattering-related fluxes is normally stronger than that of aerosols. The regression analysis would include additional independent variables such as the cloud position, optical depth, and the size and shape spectra of cloud particles, depending on the treatment of clouds in climate models. Nevertheless, Eqs (8) and (10) can be directly applied to cloudy conditions because the terms F'_{dir} and F'_{rdir} do not encounter scattering. Moreover, while only Rayleigh scattering is considered in the current regression analysis for F'_{dif}, F'_{rdif}, and F'_{coup}, Eqs. (9), (11), and (12) could serve as the first-order approximation to surface fluxes over mountains covered by clouds. Finally, we have pointed out previously that the annual mean of global average cloud amount over land surfaces is about 54% [*Warren et al*., 2007].

6. Conclusions

We have developed a 3-D radiative transfer model for mountains with a new land surface representation on the basis of a Monte Carlo photon tracing program from which the most essential radiative components are parameterized for potential application to climate models. A rugged area in the Sierra Nevada in the Western United States was chosen as a test bed, and deviations of the domain averaged solar fluxes were analyzed. Several topographic parameters were introduced as

independent variables for the multiple linear regression analysis, including the solar incident angle, elevation, slope, the sky view factor, the terrain configuration factor, as well as the standard deviation and skewness of these parameters.

Using multiple linear regression analysis, relative deviations of the five components of surface fluxes over mountains from those on an unobstructed horizontal surface are expressed by a linear combination of topographic parameters. Variation in the deviation of the direct flux is much larger than other components and generally larger than 100 W/m^2. Except when the sun is at the zenith or close to the horizon, we show that the mean solar incident angle and mean sky view factor in the regression equation can explain more than 98% of the variation, and the corresponding root mean square errors (RMSE) are generally less than 3 W/m^2. Although the explanation power is almost zero for the deviation of the direct flux with the sun at the zenith, its variation is less than 2 W/m^2, implying that the impact is of less importance. However, the RMSE can reach 10 W/m^2 when the sun is very close to the horizon.

For the deviation of the diffuse flux, about 60% of the variation can be predicted by the mean elevation, the mean solar incident angle, the mean sky view factor, and the skewness of elevation. The variation in the deviation of the diffuse flux is about 5 W/m^2, so it leads to an RMSE less than 0.5 W/m^2, smaller than that for the direct flux. The dominant factor for determining the deviations of the direct-reflected and diffuse-reflected fluxes is the terrain configuration factor with R^2 about

0.85 and 0.9, respectively. The magnitudes of the variation and RMSE for the deviation of the direct-reflected flux are respectively 1-8 and 0.08-0.5 W/m^2, depending on the position of the sun. Variation and RMSE for the deviation of the diffuse-reflected flux are consistently about 0.3 and 0.01 W/m^2, respectively. Although they are dependent on the surface albedo, their variations can be linearly scaled by using an albedo ratio factor (e.g, 0.7/0.1). The coupled flux component is more complicated because it contains photons experiencing multiple scattering and reflection. For this reason, the explanation power of the regression equation for a low albedo of 0.1 is less than those for other flux components. However, because the magnitude of the variation in the deviation of the coupled flux is only about 0.5 W/m^2, the resulting RMSE are less than 0.07 W/m^2.

For a scenario with an albedo of 0.7, the performance of the regression equation are better with R^2 larger than 0.7. Variation in the deviation of the coupled flux could reach 8 W/m^2 due to the increase in reflected energy over highly reflective surface, and the RMSE becomes 0.6 W/m^2. In this case, the terrain configuration factor becomes the dominant variable. Combining the regression equations for all five components, the departure of the solar flux over the rugged area from that of an unobstructed horizontal surface can be imposed as a correction to the horizontal-surface flux calculated by the conventional plane-parallel radiative transfer schemes. The performance of the regression equations for the coupled flux is less satisfactory; however, the error magnitude is so small that it does not affect the total flux calculation.

While the present parameterization is developed using a mean atmospheric profile at a 10×10 km^2 domain at a 1 km resolution, we have illustrated that this parameterization can be applied to different atmospheric conditions and various scales comparable to the grid size of regional climate models and GCMs. Moreover, the significant flux deviations calculated by this parameterization reveals that mountain effects are important in the modeling of surface energy balance. The spatial resolution used in the development of surface solar flux parameterization is an important issue and it is a subject requiring further investigation, Resolving the cloud and aerosol issues within the context of the parameterization of surface radiative fluxes over mountains is a challenging task, and it also requires additional in-depth theoretical and numerical investigations. Finally, we would like to point out that similar analysis could be applied to thermal infrared radiative transfer in mountains, in which the necessary parameters will include terrain information and the temperatures of surrounding mountain surfaces and the lower atmosphere.

Acknowledgments. The research of this work has been supported by NSF grants ATM-0747533 and AGS-0946315 and DOE grant DE-FG03-00ER62904. We thank Jeff Dozier and another reviewer for helpful comments, which lead to substantial improvements in the presentation of this paper.

References

Bonan, G. (2002), *Ecological Climatology: Concepts and Applications*, 678 pp., Cambridge Univ. Press, New York.

Chen, Y., A. Hall, and K. N. Liou (2006), Application of 3D solar radiative transfer to mountains, *J. Geophys. Res*., *111*, D21111,doi:10.1029/2006JD007163.

Dozier, J. (1980), A clear-sky spectral solar radiation model for snow-covered mountainous terrain, *Water Resour. Res.*, *16*, 709–718, doi:10.1029/WR016i004p00709.

Dozier, J., and J. Frew (1990), Rapid calculations of terrain parameters for radiation modeling from digital elevation data, *IEEE Trans*. *Geosci. Remote Sens*., *28*, 963-969, doi:10.1109/36.58986.

Dubayah, R., J. Dozier, and F. W. Davis (1989), The distribution of clear-sky radiation over varying terrain, *Proceedings IGARSS '89*, vol. 2, pp. 885-888, IEEE 89CH2768-0.

Dubayah, R., J. Dozier, and F. W. Davis (1990), Topographic distribution of clear-sky radiation over the Konza Prairie, Kansas, *Water Resour*. *Res*., *26*, 679–690, doi:10.1029/89WR03107.

Dubayah, R., and P. Rich (1995), Topographic solar radiation models for GIS, *Int*. *J*. *Geogr*. *Inf*. *Sci*., *9*, 405–419, doi: 10.1080/02693799508902046.

Duguay, C. (1993), Radiation modeling in mountainous terrain: Review and status, *Mt*. *Res*. *and Dev*., *13*, 339–357, doi:10.2307/3673761.

Essery, R., and D. Marks (2007), Scaling and parameterization of clear-sky solar radiation over complex topography, *J. Geophys. Res.*, *112*, D10122, doi:10.1029/2006JD007650.

Farr, T. G., P. A. Rosen, E. Caro, R. Crippen, R. Duren, S. Hensley, M. Kobrick, M. Paller, E. Rodriguez, L. Roth, D. Seal, S. Shaffer, J. Shimada, J. Umland, M. Werner, M. Oskin, D. Burbank, and D. Alsdorf (2007), The Shuttle Radar Topography Mission, *Rev. Geophys.*, *45*, RG2004, doi:10.1029/2005RG000183.

Fu, Q., and K. N. Liou (1992), On the correlated *k*-distribution method for radiative transfer in nonhomogeneous atmospheres, *J. Atmos. Sci.*, *49*, 2139–2156, doi:10.1175/1520-0469(1992)049<2139:OTCDMF>2.0.CO;2.

Geiger, R. (1965), *The Climate Near the Ground*, 611 pp., Harvard Univ. Press, Cambridge, Mass.

Gu, L., D. Baldocchi, S. B. Verma, T. A. Black, T. Vesala, E. M. Falge, and P. R. Dowty (2002), Advantages of diffuse radiation for terrestrial eco-system productivity, *J. Geophys. Res.*, *107*(D6), 4050, doi:10.1029/2001JD001242.

Gu, Y., J. Farrara, K. N. Liou, and C. R. Mechoso (2003), Parameterization of cloud-radiation processes in the UCLA general circulation model, *J. Climate*, *16*, 3357–3370, doi:10.1175/1520-0442(2003)016<3357:POCPIT>2.0.CO;2.

Gu, Y., K. N. Liou, Y. Xue, C. R. Mechoso, W. Li, and Y. Luo (2006), Climatic effects of different aerosol types in China simulated by the UCLA atmospheric general circulation model, *J.*

Geophys. *Res*., *111*, D15201, doi:10.1029/2005JD006312.

Hay, J. E., and D. C. McKay (1985), Estimating solar irradiance on inclined surfaces: a review and assessment of methodologies, *Int*. *J*. *Sol*. *Energy*, *3*, 203–240, doi:10.1080/01425918508914395.

Jenness, J. S. (2004), Calculating landscape surface area from digital elevation models, *Wildlife Soc*. *Bull*., *32*(3), 829–839, doi:10.2193/0091-7648(2004)032[0829:CLSAFD]2.0.CO;2.

Liou, K. N., W.-L. Lee, and A. Hall (2007), Radiative transfer in mountains: Application to the Tibetan Plateau, *Geophys*. *Res*. *Lett*., *34*, L23809, doi:10.1029/2007GL031762.

Miesch, C., X. Briottet, Y. H. Herr, and F. Cabot (1999), Monte Carlo approach for solving the radiative transfer equation over mountainous and heterogeneous areas, *Appl*. *Opt*., *38*, 7419–7430, doi:10.1364/AO.38.007419.

Müller, M. D., and D. Scherer (2005), A grid- and subgrid-scale radiation parameterization of topographic effects for mesoscale weather forecast models, *Mon*. *Weather Rev*., *133*, 1431–1442, doi:10.1175/MWR2927.1.

Olyphant, G. A. (1986), The components of incoming radiation within a mid-latitude alpine watershed during the snowmelt season, *Arct*. *Alp*. *Res*., *18*, 163–169, doi:10.2307/1551125.

Wang, Q., J. Tenhunen, M. Schmidt, D. Otieno, O. Kolcun, and M. Droesler (2005), Diffuse PAR irradiance under clear skies in complex alpine terrain, *Agric*. *For*. *Meteorol*., *128*, 1–15,

doi:10.1016/j.agrformet.2004.09.004.

Warren, S. G., R. M. Eastman, and C. J. Hahn (2007), A survey of changes in cloud cover and cloud types over land from surface observations, 1971-96, *J. Climate*, *20*, 717–738, doi:10.1175/JCLI4031.1.

Table Captions

Table 1. Intercepts and Regression Coefficients for Eqs. (8) and (9).

Table 2. R^2 for Eqs. (8), (9), (10), (11), and (12).

Table 3. Intercepts and Regression Coefficients for Eqs. (10) and (11).

Table 4. Intercepts and Regression Coefficients for Eq. (12) for Two Surface Albedos of 0.1 and 0.7.

Figure Captions

Figure 1. Maps of the elevation (left, unit in meter) and slope (right, unit in degree) in the Sierra Nevada area.

Figure 2. A schematic representation of flux components received by the target on an inclined surface in a mountainous area: (1) direct flux, (2) diffuse flux, (3) direct-reflected flux, (4) diffuse-reflected flux, and (5) coupled flux. The solar incident angle θ_i, the sky view factor V_d and the terrain configuration factor C_t are also shown.

Figure 3. Comparison between the results from the Monte Carlo photon tracing simulation (real values) and the multiple linear regression analysis (predicted values) for the direct flux (left panels) and the diffuse flux (right panels).

Figure 4. Vertical distribution of the downward diffuse fluxes over an unobstructed horizontal surface with elevation of zero for $\mu_0 = 0.1$, 0.4, and 1.0.

Figure 5. As in Figure 3, but for the direct-reflected flux (left panels) and diffuse-reflected flux (right panels).

Figure 6. As in Figure 3, but for the coupled flux with a surface albedo of 0.1 (left panels) and a surface albedo of 0.7 (right panels).

Table 1. Intercepts and Regression Coefficients for Eqs. (8) and (9).

	Direct Flux			Diffuse Flux				
μ_0	a_1	b_{11}	b_{12}	a_2	b_{21}	b_{22}	b_{23}	b_{24}
0.10	-2.91×10^{-2}	3.07×10^{-1}	3.90×10^{-2}	-7.28×10^{-3}	9.64×10^{-3}	2.24×10^{-3}	1.19×10^{-2}	-4.15×10^{-3}
0.25	-1.94×10^{-3}	1.56×10^{-1}	-1.69×10^{-3}	-1.33×10^{-3}	1.07×10^{-2}	3.53×10^{-3}	8.63×10^{-3}	-3.89×10^{-3}
0.40	-1.05×10^{-4}	9.49×10^{-2}	-6.99×10^{-3}	2.75×10^{-4}	1.09×10^{-2}	5.25×10^{-3}	7.16×10^{-3}	-3.95×10^{-3}
0.55	-1.40×10^{-4}	6.32×10^{-2}	-7.11×10^{-3}	7.40×10^{-4}	1.06×10^{-2}	6.62×10^{-3}	6.40×10^{-3}	-3.90×10^{-3}
0.70	-1.29×10^{-4}	4.27×10^{-2}	-7.15×10^{-3}	9.12×10^{-4}	1.02×10^{-2}	7.07×10^{-3}	5.55×10^{-3}	-3.67×10^{-3}
0.85	-6.15×10^{-5}	2.65×10^{-2}	-7.11×10^{-3}	7.16×10^{-4}	9.59×10^{-3}	6.34×10^{-3}	4.57×10^{-3}	-3.61×10^{-3}
1.00	-8.32×10^{-5}	5.10×10^{-5}	-2.65×10^{-5}	7.64×10^{-4}	8.01×10^{-3}	0	5.66×10^{-3}	-3.10×10^{-3}

Table 2. R^2 for Eqs. (8), (9), (10), (11), and (12).

	F_{dir}	F_{dif}	F_{rdir}	F_{rdif}	F_{coup}	
μ_0					alb=0.1	alb=0.7
0.10	0.749	0.608	0.442	0.893	0.484	0.473
0.25	0.988	0.611	0.823	0.896	0.676	0.710
0.40	0.999	0.612	0.858	0.895	0.648	0.748
0.55	0.998	0.631	0.864	0.893	0.548	0.756
0.70	0.997	0.635	0.863	0.892	0.425	0.755
0.85	0.991	0.625	0.860	0.891	0.263	0.754
1.00	0.006	0.575	0.864	0.887	0.168	0.766

Table 3. Intercepts and Regression Coefficients for Eqs. (10) and (11).

	Direct-Reflected Flux				Diffuse-Reflected Flux			
μ_0	a_3	b_{31}	b_{32}	b_{33}	a_4	b_{41}	b_{42}	b_{43}
0.10	2.76×10^{-3}	1.15×10^{-3}	1.25×10^{-4}	-8.12×10^{-5}	2.54×10^{-3}	1.17×10^{-3}	2.15×10^{-4}	-1.20×10^{-4}
0.25	2.62×10^{-3}	1.27×10^{-3}	1.71×10^{-4}	-1.02×10^{-4}	2.57×10^{-3}	1.20×10^{-3}	2.17×10^{-4}	-1.26×10^{-4}
0.40	2.55×10^{-3}	1.23×10^{-3}	1.97×10^{-4}	-1.05×10^{-4}	2.58×10^{-3}	1.22×10^{-3}	2.21×10^{-4}	-1.27×10^{-4}
0.55	2.51×10^{-3}	1.20×10^{-3}	2.11×10^{-4}	-1.06×10^{-4}	2.58×10^{-3}	1.22×10^{-3}	2.20×10^{-4}	-1.33×10^{-4}
0.70	2.48×10^{-3}	1.18×10^{-3}	2.19×10^{-4}	-1.07×10^{-4}	2.58×10^{-3}	1.22×10^{-3}	2.22×10^{-4}	-1.34×10^{-4}
0.85	2.47×10^{-3}	1.16×10^{-3}	2.26×10^{-4}	-1.07×10^{-4}	2.57×10^{-3}	1.21×10^{-3}	2.21×10^{-4}	-1.36×10^{-4}
1.00	2.46×10^{-3}	1.16×10^{-3}	2.25×10^{-4}	-1.08×10^{-4}	2.57×10^{-3}	1.22×10^{-3}	2.27×10^{-4}	-1.30×10^{-4}

Table 4. Intercepts and Regression Coefficients for Eq. (12) for Two Surface Albedos of 0.1 and 0.7.

	Coupled Flux (Albedo = 0.1)				Coupled Flux (Albedo = 0.7)			
μ_0	a_5	b_{51}	b_{52}	b_{53}	a_5	b_{51}	b_{52}	b_{53}
0.10	-1.01×10^{-2}	3.76×10^{-2}	-4.07×10^{-3}	2.27×10^{-3}	4.74×10^{-2}	3.54×10^{-2}	2.73×10^{-2}	7.46×10^{-3}
0.25	-1.46×10^{-2}	2.91×10^{-2}	-8.93×10^{-4}	2.19×10^{-3}	3.94×10^{-2}	2.71×10^{-2}	2.99×10^{-2}	4.08×10^{-3}
0.40	-1.74×10^{-2}	1.96×10^{-2}	-1.40×10^{-3}	1.52×10^{-3}	3.65×10^{-2}	1.80×10^{-2}	2.88×10^{-2}	4.11×10^{-3}
0.55	-1.88×10^{-2}	1.35×10^{-2}	-2.15×10^{-3}	1.51×10^{-3}	3.43×10^{-2}	1.20×10^{-2}	2.76×10^{-2}	4.83×10^{-3}
0.70	-1.96×10^{-2}	9.02×10^{-3}	-2.86×10^{-3}	-6.44×10^{-4}	3.35×10^{-2}	7.76×10^{-3}	2.68×10^{-2}	5.05×10^{-3}
0.85	-2.00×10^{-2}	4.97×10^{-3}	-3.43×10^{-3}	-5.79×10^{-4}	3.29×10^{-2}	4.07×10^{-3}	2.60×10^{-2}	5.17×10^{-3}
1.00	-1.94×10^{-2}	0	-4.52×10^{-3}	-7.52×10^{-4}	3.26×10^{-2}	0	2.46×10^{-2}	4.94×10^{-3}

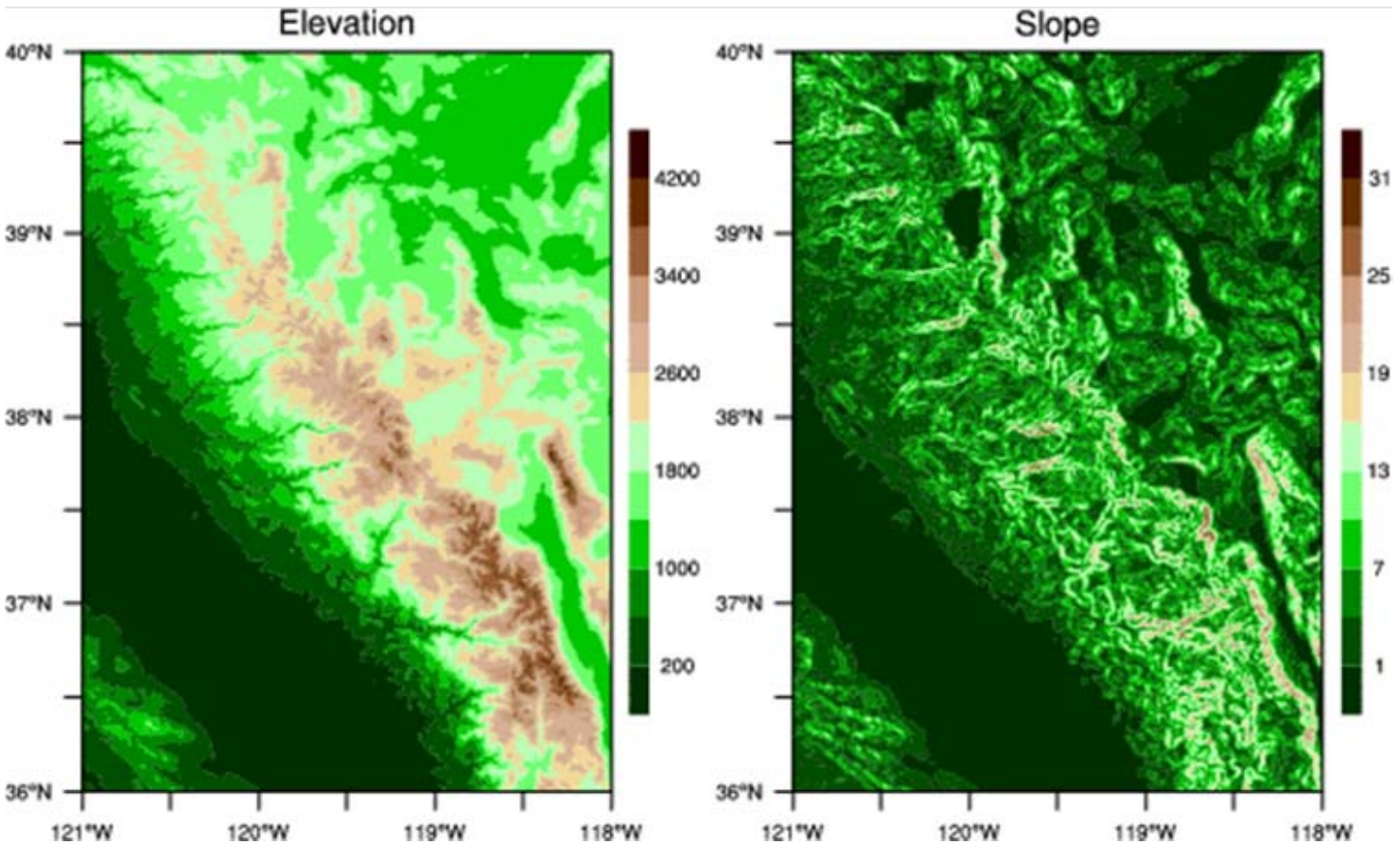

Figure 1. Maps of elevation (left, unit in meter) and slope (right, unit in degree) in the Sierra Nevada area.

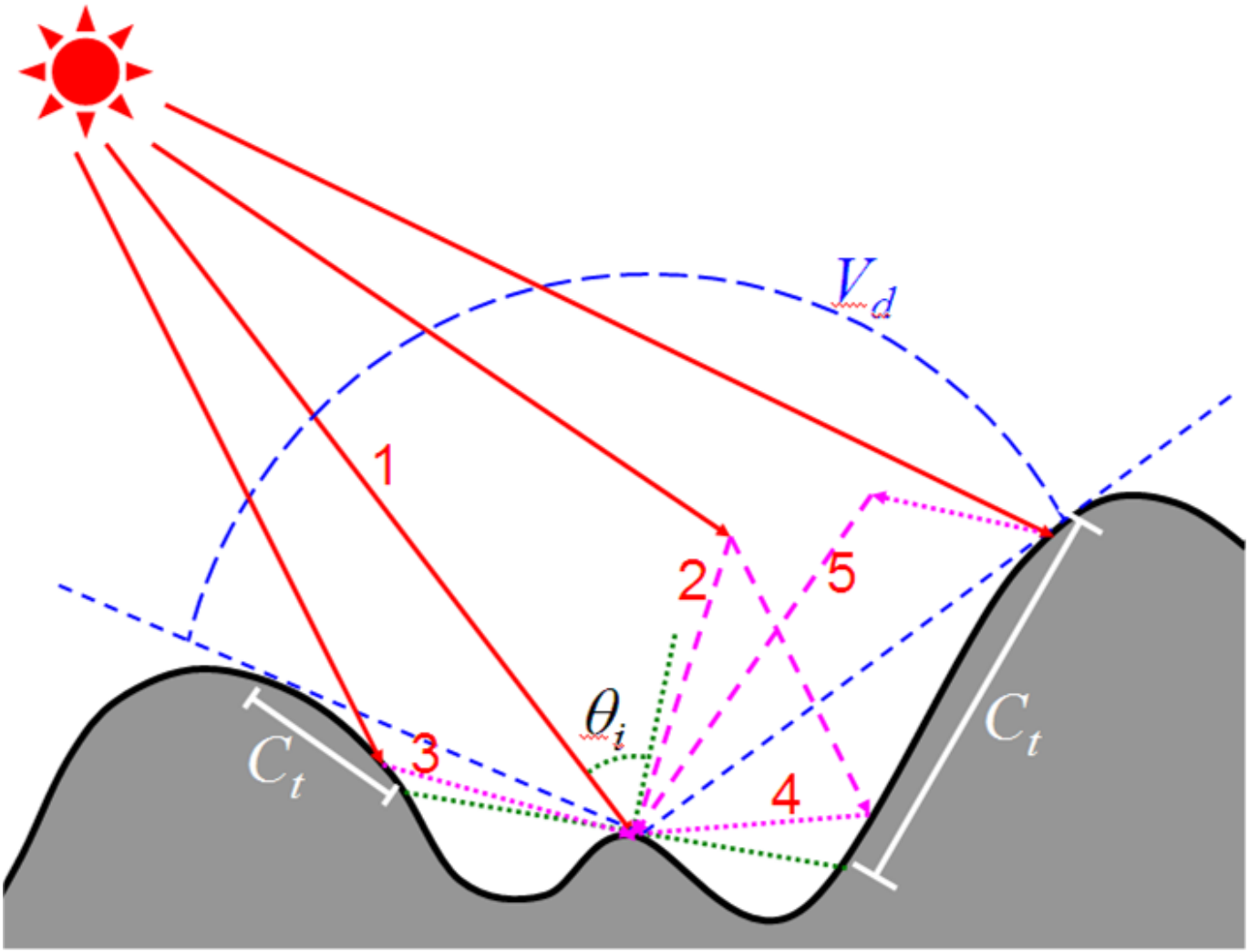

Figure 2. A schematic representation of flux components received by the target on an inclined surface in a mountainous area: (1) direct flux, (2) diffuse flux, (3) direct-reflected flux, (4) diffuse-reflected flux, and (5) coupled flux. The solar incident angle θ_i, sky view factor V_d and terrain configuration factor C_t are also shown.

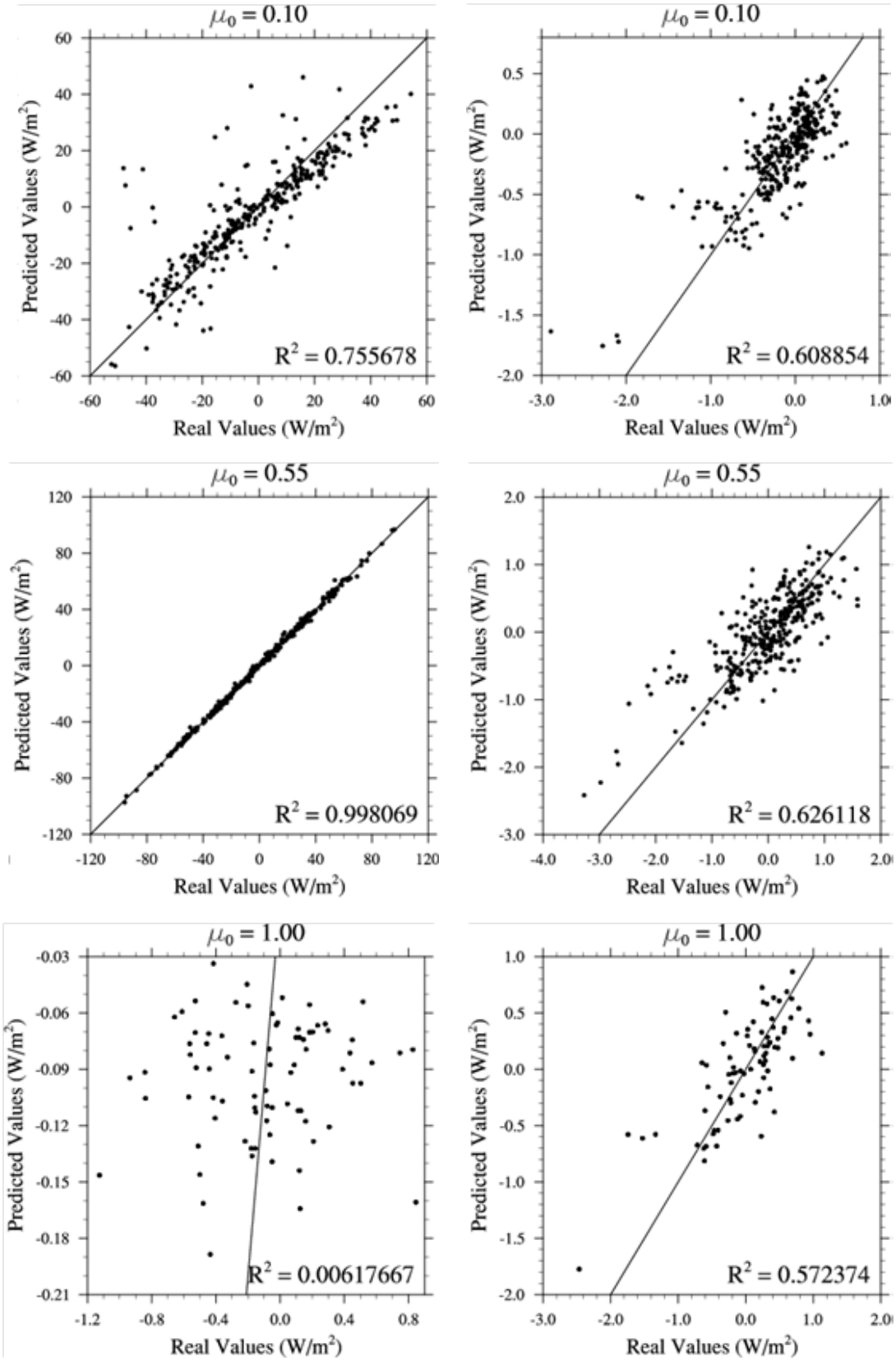

Figure 3. Comparison between the results from Monte Carlo simulation (real values) and from multiple linear regression (predicted values) for the direct flux (left panels) and diffuse flux (right panels).

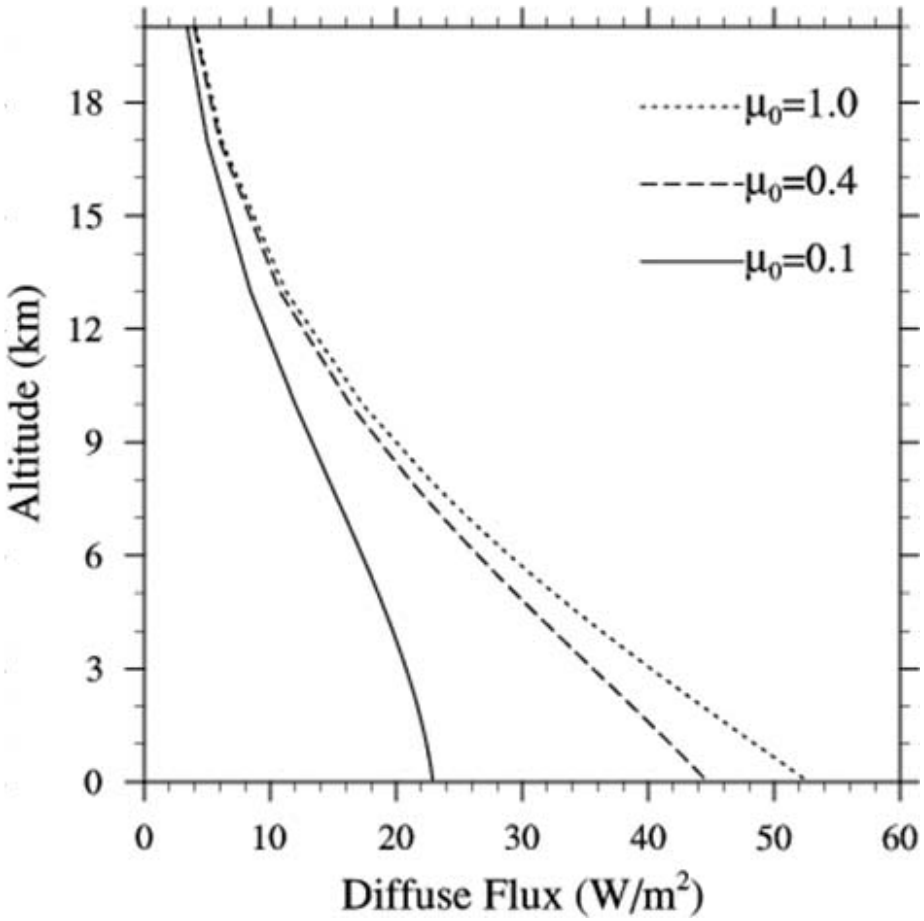

Figure 4. Vertical distribution of the downward diffuse fluxes over an unobstructed horizontal surface with elevation of zero for μ_0 = 0.1, 0.4, and 1.0.

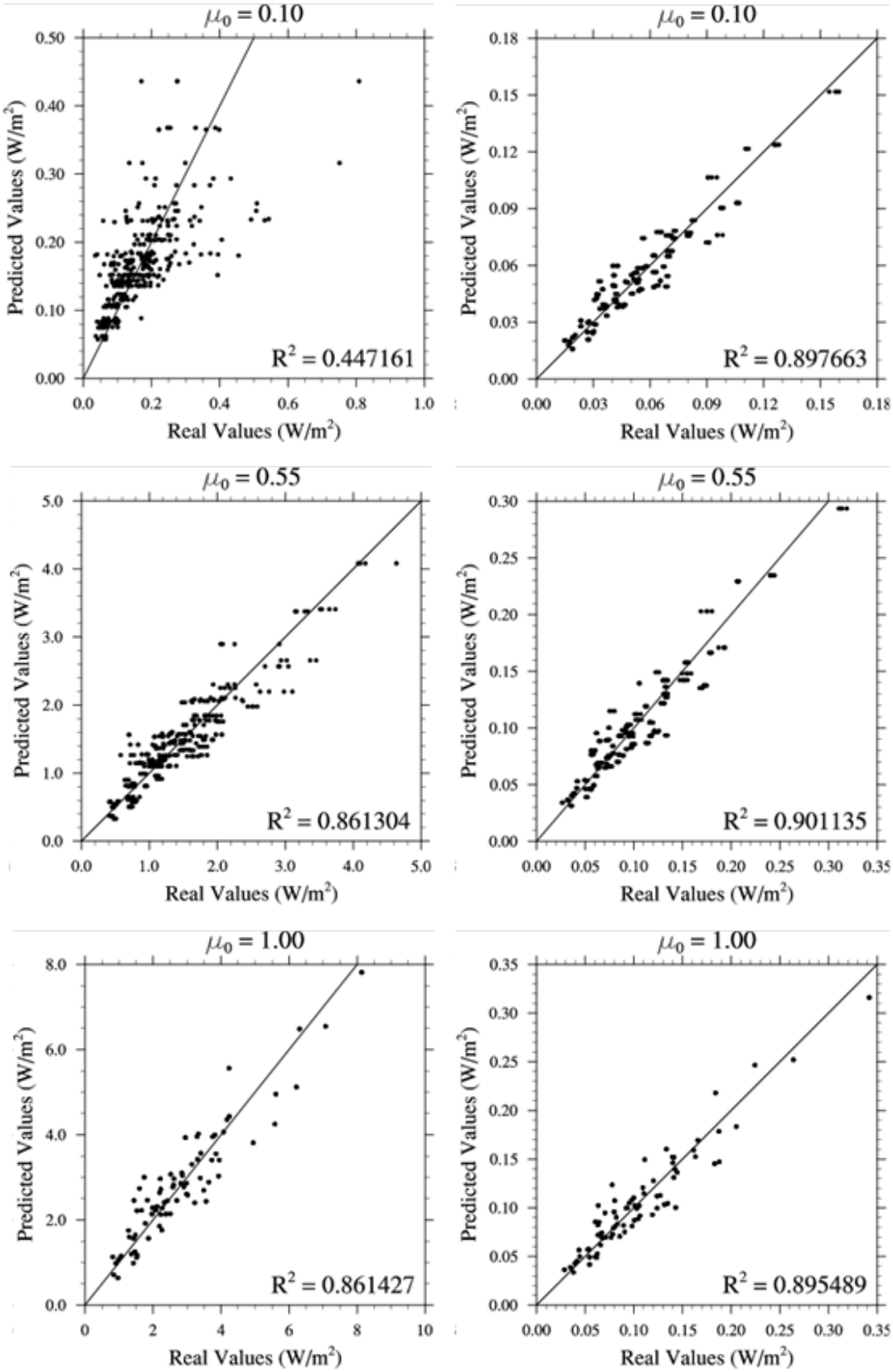

Figure 5. As in Figure 3, but for the direct-reflected flux (left panels) and diffuse-reflected flux (right panels).

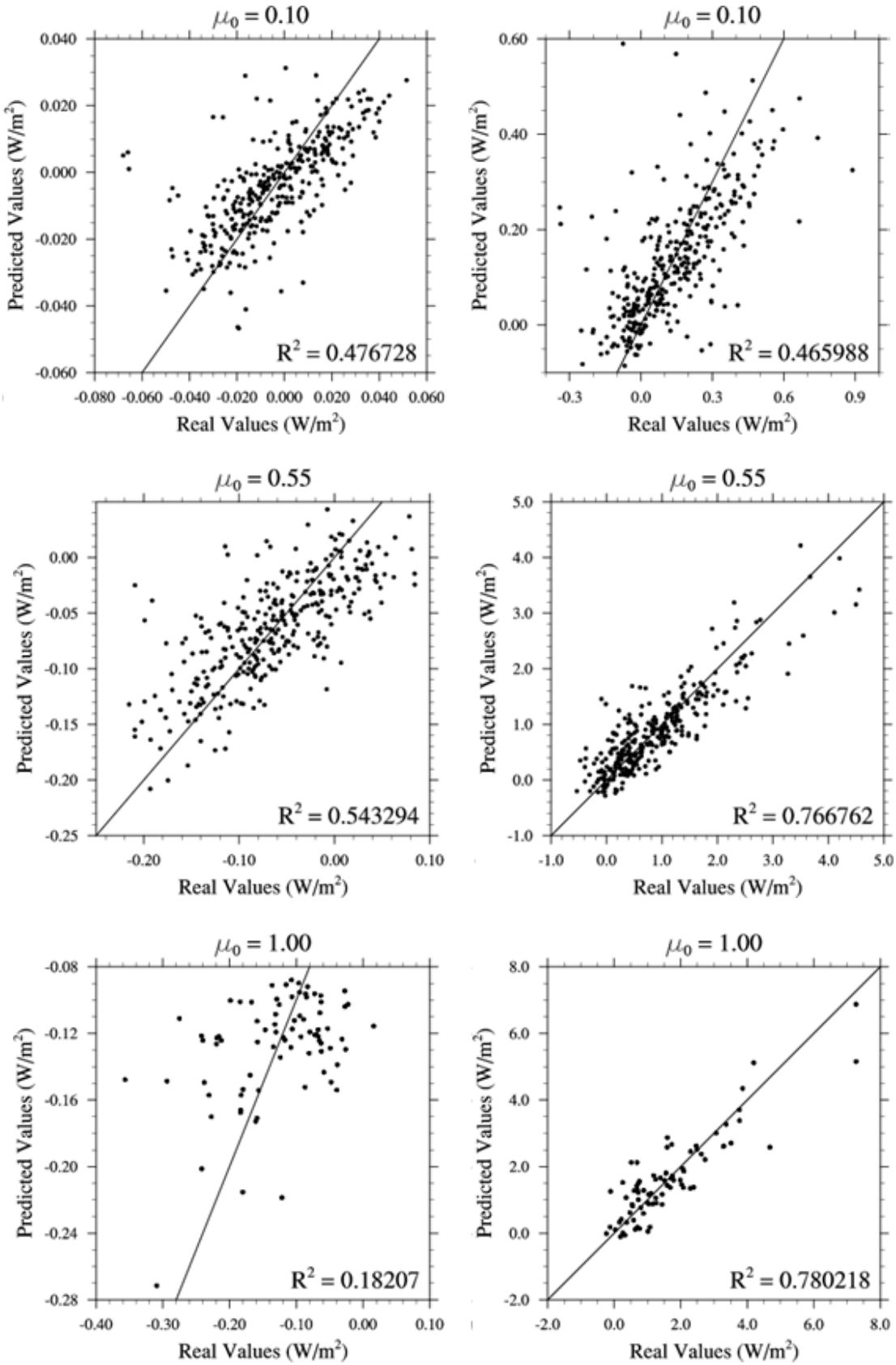

Figure 6. As in Figure 3, but for the coupled flux with surface albedo of 0.1 (left panels) and albedo of 0.7 (right panels).